# RECENT IMPROVEMENTS IN THE SPACE CODE

**Kyung Doo Kim, S. W. Lee , S. W. Bae, B. J. Kim, J. S. Heo, J. H. Lee,**
**B.U. Bae and B. D. Chung**
Korea Atomic Energy Research Institute (KAERI)
1045 Deadeok-daero, Yuseong, Daejeon, 305-353, Korea

kdkim@kaeri.re.kr; nuclist@kaeri.re.kr; bswon@kaeri.re.kr; byoungjae@kaeri.re.kr;
jheo@kaeri.re.kr; leejonghyuk@kaeri.re.kr; bubae@kaeri.re.kr; bdchung@kaeri.re.kr

## ABSTRACT

The SPACE (the Safety and Performance Analysis Code for Nuclear Power Plants) code is under develop ment to be used for licensing pressurized water reactor design. The SPACE code adopts advanced physica l modeling of two-phase flows, mainly two-phase three-field models which comprise gas, continuous liqu id, and droplet fields but it has a capability to handle the classical two-phase two-field model by user's selection. It has the capability to simulate 3D effects by the use of structured and/or non-structured meshe s. In this paper, recent advances in the SPACE code will be briefly presented. First, the model improvements for multi-dimensional applications are introduced with a few validation results. Second, optional two-phase two-fluid model development activities are described. The comparison of calculation results with two-phase three-fluid model case is also presented. Third, nonphysical phasic velocities for a dispersed field were corrected by improving pressure drop by wall drag and from loss. Fourth, an improved CHF model for pool boiling condition based on instability theory is also introduced. Fifth, a two group interfacial area transport model is incorporated to predict dispersed liquid interfacial area. Finally, uncertainty quantification based on data assimilation technique is demonstrated.

**KEYWORDS**
two-phase three-field model, multi-dimensional, interfacial area transport, uncertainty quantification

## 1. INTRODUCTION

The current safety analysis code used for nuclear reactor design relies on foreign vendor supplied safety analysis codes which were developed in early 1970s and no more major improvement has been made. To replace the outdated foreign vendor codes, SPACE code development program was launched in 2006 and has been successfully preceded since then to develop a best-estimate thermal-hydraulics system analysis code. Before SPACE code development program, KAERI has an experience to develop a best-estimate thermal-hydraulic code, named MARS. MARS code has been developed MARS (Multi-dimensional Analysis of Reactor Safety) code has been developed for the realistic multi-dimensional thermal-hydraulic system analysis of light water reactor transients since 1997. The backbones of MARS are the RELAP5/MOD3.2.1.2 and the COBRA-TF codes of USNRC. MARS is used as an audit tool for nuclear regulatory institute. SPACE code [1] is developing based on a multi-dimensional two-fluid, three-field model. A separate set of mass, energy and momentum equations are solved for each fields (gas, continuous liquid, and dispersed droplet), with closure relations to account for mass, energy and momentum transfer between fields. Also, SPACE code is written in C++ programming language for the new generation of engineers who are more comfortable with C++ than FORTRAN language. Several research and industrial organizations in Korea are participated in the collaboration of the SPACE code development program. SPACE code development program is divided in 3 development stages for 10

years. During the first stage, the development of the demonstration version and the basic verification work was completed. In the second stage, it is focused to validate SPACE code by using the SET and IET problems. The validation had been performed for 1D parts of SPACE code since the project schedule is too tight to validate all 1D and 3D capabilities. SPACE code development program is in last stage. During this stage, the topical report was submitted for regulatory review. Regulatory review is in progress for 1D part of SPACE code. During this stage, we are also improving the SPACE code to enhance its performance including validation of 3D capability. In this paper, recent advances in the SPACE code will be briefly introduced.

## 2. MODELS AND VALIDATION FOR MULTI-DIMENSIONAL ANALYSIS

For SPAEC code, each field equation is discretized by applying the finite volume method to the very unique SPACE mesh system which naturally encompasses various three-dimensional structured and or non-structured mesh systems, as well as one-dimensional pipe. The SPACE I/O systems are changed to accept the multi-dimensional geometry descriptions for both Cartesian and cylindrical coordinates. For the use of the models and correlations, the hydraulic diameter for a multi-dimensional cell is the root-mean-square of three directional hydraulic diameters for each axis. The characteristic length of the multi-dimensional cell is calculated by the same manner. The characteristic length of the multi-dimensional cell is used to obtain the scalar terms of the mass and energy equations. The determination of flow regime is conducted by using the inclined factor of flow as in Eq. (1), which consists of the vertical velocity component to root-mean-square of the three dimensional velocity components ratio. The inclined factor for the 1-D system is directly obtained from geometry input. But for the multi-dimensional system, the cell inclination is not consistent to the flow inclination. The flow inclined factor of multi-dimensional cell is calculated by the following equations.

$$\mathrm{f_{incl}} = \left| \frac{v_{zs}}{\sqrt{v_{xs}^2 + v_{ys}^2 + v_{zs}^2}} \right| \tag{1}$$

For each direction k,

$$v_{ks} = \alpha_g v_{g,k} + \alpha_l v_{l,k} + \alpha_d v_{d,k} \tag{2}$$

The flow regime is characterized by horizontal flow if the value of Eq. (1) is under 1/3 and uses horizontal flow regime map. If it is over 2/3, the flow is considered as vertical flow. Interface properties, i.e., interface heat transfer, interface friction, are found by using vertical flow regime map. Between 1/3 and 2/3 regions, interface properties are interpolated.

Several simple conceptual problems are used to verify the SPACE multi-dimensional component. Among them, phase separation problem and 1D connection problem are described here.

1D connection problem is performed to show the momentum integrity of SPACE multi-dimensional component. A long vertical pipe is divided to three parts, which is 1D pipe followed by multi-dimensional component and 1D pipe again as shown in Fig. 1. The grid number for the x, y, z direction of the multi-dimensional component is 1×1×12. A single phase flow is injected from the bottom boundary volume. The flow area is 0.01 $m^2$ for both 1D and multi-dimensional cells. The conditions of the bottom injection flow are 150 bar, 600 K and 10.0 kg/s. The wall friction model for the 1D and multi-dimensional component works sound and provides the same friction pressure drop for the calculation domain. The connection faces, C250 and C350, show the reasonable pressure drops and velocity values.

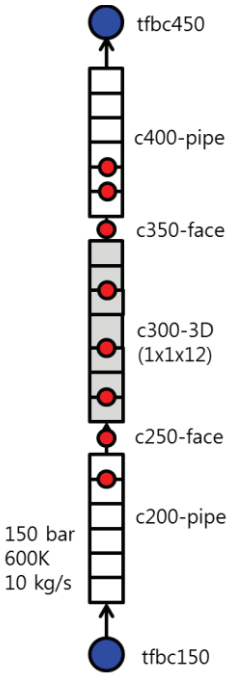


| Face position | Velocity (m/s) |
|---|---|
| c200-f05 | 1.51715 |
| c250-f01 | 1.51715 |
| c300-fz1-1-01 | 1.51715 |
| c300-fz1-1-03 | 1.51716 |
| c300-fz1-1-05 | 1.51717 |
| c300-fz1-1-07 | 1.51718 |
| c300-fz1-1-09 | 1.51719 |
| c300-fz1-1-11 | 1.51720 |
| c350-f01 | 1.51720 |
| c400-f01 | 1.51721 |
| c400-f02 | 1.51722 |

**Figure 1. 1D and multi-D connection pipe flow problem**

The phase separation problem is conducted for the 3×1×19 grid multi-D component as shown in Fig. 2. The node size is 0.1 m for all directions. The whole calculation domain is initially filled with mixture of water and steam. The initial void fraction is set as 0.4. As the calculation goes on, water accumulates at the bottom region of the 3x1x19 multi-D component. While the steam gathers in the top region. Finally, all 12$^{th}$ vertical nodes become stratified and void fraction of those is 0.6. Below the 12$^{th}$ vertical node, it is single phase water. As the other case, initial void fraction is set as 0.8. At this time, final stratified node is observed in the 4$^{th}$ vertical region. The void fraction of the 4$^{th}$ vertical nodes is 0.2.

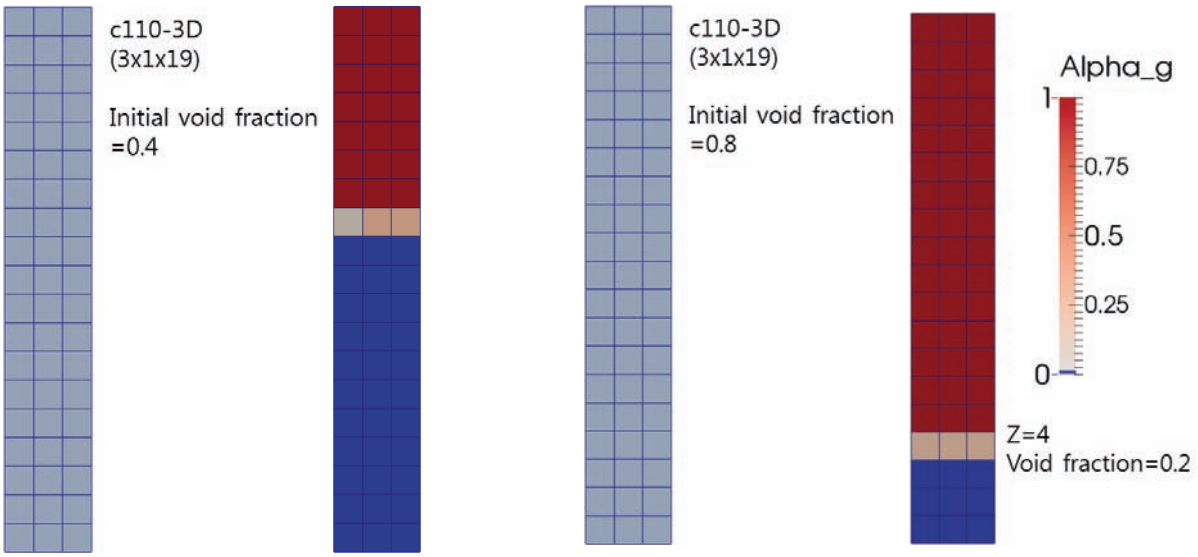


(a) Initial void fraction 0.4 (b) Initial void fraction 0.8

**Figure 2. Phase separation problem**

After simple verification, SPACE multi-D component used to assess the RPI 2D slab air-water void distribution experiment [2]. Similar to the phase separation problem, RPI 2D slab problem is modeled as the vertical slab geometry. The slab height and width are 0.9144 by 0.9144 m. the depth of slab is 0.0127 m. There are 4 inlet and outlet port slits. The liquid injection port is arranged at the right top of the slab. The liquid-air mixture injection port is located at the bottom middle of the slab. The gage pressure is under 0.5 bar level. Figure 3 and table 1 show the RPI 2D slab port configuration and injection conditions.

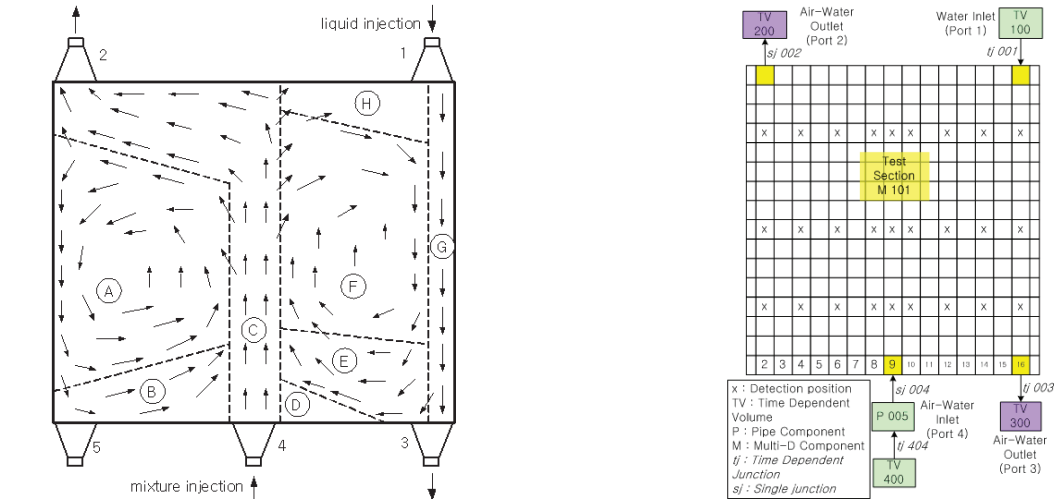


(a) RPI 2D slab port configuration (b) SPACE modeling of 2D slab

**Figure 3. RPI 2D slab configuration and SPACE modeling**

**Table 1. RPI 2D slab port injection and boundary conditions (1AN4)**

| Pressure (kPa) | Temperature (K) | Port 1 Liquid flow (kg/s) | Port 4 Liquid flow (kg/s) | Port 4 Quality (%) | Port4 Assumed air flow (kg/s) | Port 3 Assumed Liq. flow (kg/s) |
|---|---|---|---|---|---|---|
| 131.6 | 298.0 | 0.085 | 0.085 | 0.6 | 0.002 | 0.085 |

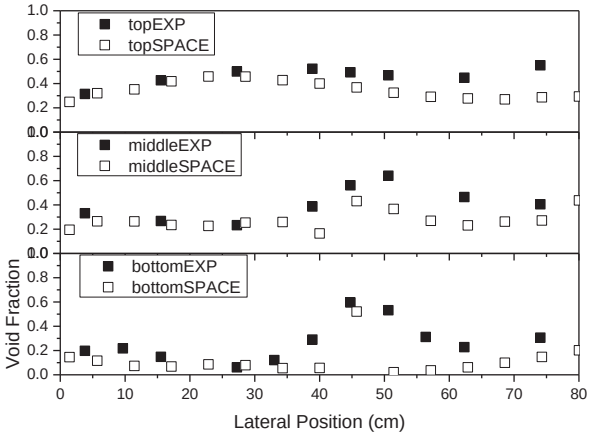


**Figure 4. Void fraction prediction of SPACE**

The void fraction distribution predicted by SPACE codes are shown in Fig. 4 for the bottom, middle, and top heights. SPACE under-estimates the void fraction in the right half region of the slab. It may be caused by the insufficient modeling of the interfacial friction for the horizontal and counter flow movement of the bubbles. These results are quantitatively not sufficient to validate, but in qualitative view points, show reasonable void fraction distributions.

## 3. OPTIONAL TWO-PHASE TWO-FLUID MODEL

The main objective of SPACE 6 equation platform is to enhance the calculation speed. According to the purpose, droplet field calculation processes were totally removed from the hydraulic models. The 6 equation sets are activated by option card input by user. The I/O systems and solver programs are modified to eliminate the droplet related terms. Further, models and correlations are modified to eliminate the droplet effects. In order to these, additional functions except the droplet related terms are made and adapted for whole models and correlations. At first, flow regime determination is modified. In the 9 equation system, SPACE does not distinguish the annular and dispersed flow regime. There are only annular flow regimes that include liquid film or not. In the 6 equation system, the dispersed flow regime appears when the void fraction is over 0.95. At that instance, the liquid fraction is forced to be divided into film and imaginary induced droplet. The induced droplet is not a real droplet. It takes only the effect of droplet.
The calculation speed of 9 and 6 equation systems of SPACE are compared as in the table 2. The simple 2 phase problem is about vertical pipe flowing water and steam mixture. Pipe is modeled by 20 nodes. The CHF problem consists of 20 node vertical pipe and heat structure that transfers high heat fluxes enabling critical heat flux condition. The reflood problem is added a subcooled liquid flow injected from the bottom of vertical 20 node pipe and heat structure.

**Table 2. Calculation time comparisons between 9 and 6 equation systems of SPACE**

| problem | Simple 2 phase flow | CHF problem | Reflood problem |
|---|---|---|---|
| Problem time | 50 | 50 | 200 |
| 9 equation | 5.897 | 6.645 | 469.579 |
| 6 equation | 4.711 | 5.959 | 449.470 |
| Time difference | -1.186 | -0.686 | -20.109 |

For the FLECHT-SEASET 31504 test case is selected to compare the calculation results between 9 and 6 equation systems. As shown in Fig. 5, the peak temperature at the 6 and 10 ft heights for 6 equation case are higher than the results for 9 equation case. It may cause that the droplet fraction (or liquid interface area) in 6 equation case is predicted smaller than that in 9 equation case. The quench times for each elevation are not affected much with respect to the 9 or 6 equations.

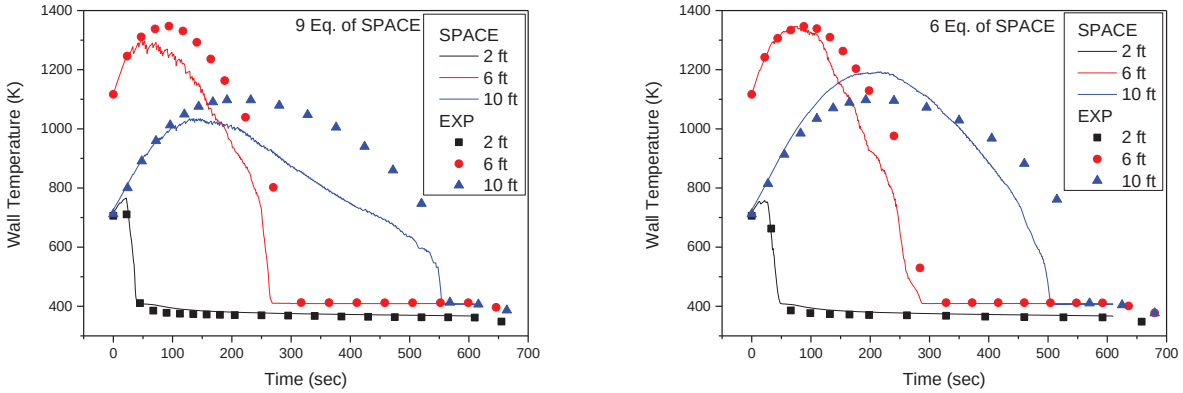


(a) Wall temperature predicted by 9 eq. (b) Wall temperature predicted by 6 eq.

**Figure 5. Wall temperature prediction of SPACE for the FLEACHT-SEASET 31504 experiment**

## 4. PRESSURE DROP TERMS FOR WALL FRAG AND FORM LOSS

Recently, we brought light to the wall drag term for dispersed flows, examining the averaged momentum equations based on the equation of a solid/fluid particle motion [3]. The wall drag term on the bubble phase accounts for the interaction between the stresses of the undisturbed water and the bubble phase. As a result, the total pressure drop by the wall friction of the continuous phase must be apportioned to each phase in proportion to each phase fraction. By doing so, the relative velocity of the dispersed phase against the continuous phase can be correctly predicted in a pipe, contraction, and expansion.

In addition, a new form loss model was proposed for dispersed flows. According to the existing form loss model ( $\Delta p = 0.5K\alpha_k \rho_k |v_k| v_k$ ), the bubble is predicted to be faster than water even for a fully-developed flow. However, the droplet is predicted to be slower than gas. The incorrect predictions are because the existing form loss model is based on two continua concept. To solve this deficiency, the total momentum loss by the continuous phase is first calculated. After that, the total momentum loss is apportioned to each phase in proportion to each phase fraction. This partitioning approach is consistent with the wall drag partitioning. This is not surprising because the form loss is merely a different expression of the wall drag [4].

Figure 6 shows the velocity prediction in the horizontal channel. The flow area is reduced at $x = 1.2$ m. When the wall drag force is not enforced on the bubble, the bubble is predicted to be higher than water everywhere. However, when the total wall drag is apportioned to each phase in proportion to each phase fraction, the two velocities equalize in the channel with constant flow area. The bubble velocity is well predicted in the contraction region; the bubble is faster than the water. The relative velocity of the bubble phase against the water is reversed in the expansion region. **Figure 7** shows the velocity prediction in the channel covering the lower plenum to the core. The flow area is reduced at $x = 0$ m (core inlet). There are nine spacer grids with a K-factor of 1.22 in the core. The flow area remains constant in the core. The existing form loss model was used. As seen, the bubble is predicted to be higher than water at every spacer grids. If the form loss model is corrected, two velocities equalize (the result is now shown here).

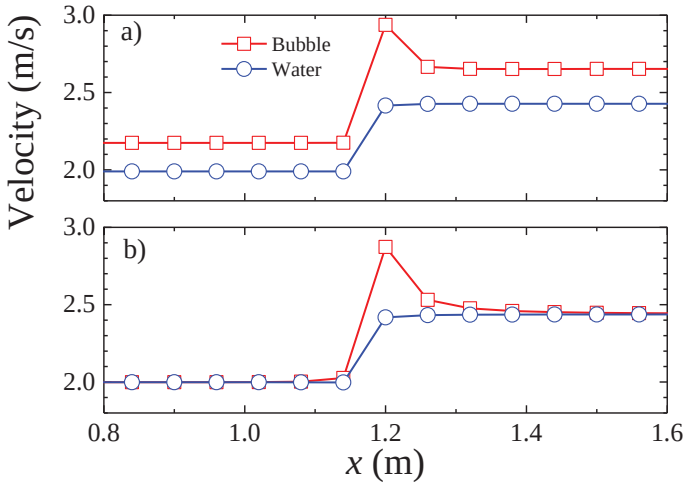


**Figure 6. Bubbly flow in the contraction: a) no wall drag on the bubble phase and b) new model**

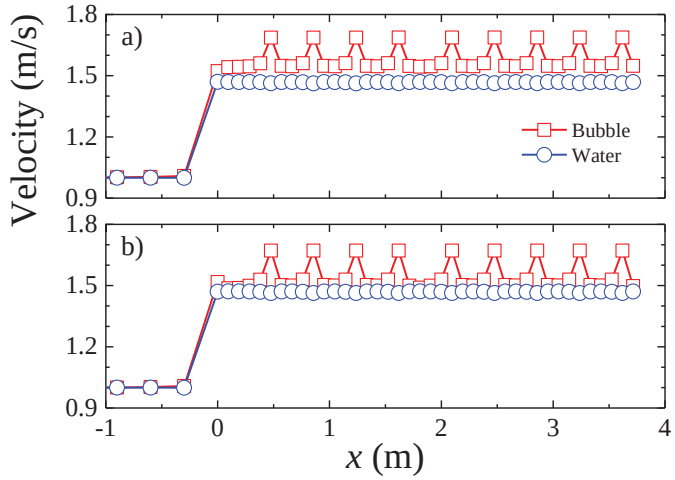


**Figure 7. Horizontal bubbly flow when the existing form loss model is used.**

## 5. HYDRODYANMIC MODEL FOR CRITICAL HEAT FLUX

The existing critical heat flux(CHF) models have been developed using the results of the interfacial instabilities for inviscid fluids. However, as the pressure increases, the viscosities of vapor and liquid become closer, and thus the effect of fluid viscosities cannot be ignored. Recently, Kim [5] considered the effects of fluid viscosity and phase change on the Rayleigh-Taylor instability, and showed that for film boiling, the gas film is thin enough that the most unstable wavelength is $\lambda_d = 2\pi(2\sigma/(\Delta\rho g))^{1/2}$. The reduction of the most unstable wavelength improved the prediction accuracies of two existing models **[6-7].**

In addition, we further modified Zuber`s model, utilizing the circular jet instabilities for viscous potential fluids. According to the theory of viscous potential theory, the motion of fluids are solved by the unsteady Bernoulli`s equation (potential flow)**[8].** However, the potential flow does not imply the viscosity is identically zero. The effect of viscosity is entered though the balance of normal pressures at the interface.

The CHF can be formulated as follows.

$$q_{\max} = \frac{\pi}{16}\rho_g^{1/2} L U_g \tag{3}$$

where $\rho_g$, $L$, and $U_g$ are gas density, latent heat, and gas velocity, respectively. Funada and his co-workers [7] conducted a stability analysis for a circular fluid jet into another fluid. The critical relative velocities between gas and liquid is given by

$$U_c^2 = \frac{\sigma(\beta_g\mu_g + \beta_f\mu_f)^2}{\alpha_g\rho_g\beta_f^2\mu_f^2 + \alpha_f\rho_f\beta_g^2\mu_g^2}\left(k_c - \frac{1}{R^2 k_c}\right) \tag{4}$$

Using the conservation of mass,

$$U_f = -\frac{\pi}{16-\pi}\frac{\rho_g}{\rho_f}U_g \tag{5}$$

Combined the above equation with Eqs. (3) and (4), we obtain the modified hydrodynamic CHF model based on the viscous potential flow as follows:

$$\frac{q_{\max}}{\rho_g^{1/2} L(\sigma\Delta\rho g)^{1/4}} = \frac{\pi}{16}\left(\gamma - \frac{2}{\pi^2\gamma}\right)^{1/2} \frac{(16-\pi)\rho_f}{\pi\rho_g + (16-\pi)\rho_f} \frac{\rho_g^{1/2}(\beta_g\mu_g + \beta_f\mu_f)}{(\alpha_g\rho_g\beta_f^2\mu_f^2 + \alpha_f\rho_f\beta_g^2\mu_g^2)^{1/2}} \tag{6}$$

Since $\alpha_g$, $\alpha_f$, $\beta_g$, and $\beta_f$ depends on $\gamma$, there is only one unknown parameter $\gamma$. The value of $\gamma$ was determined by matching the predicted CHF at atmospheric pressure to Lienhard and Dhir's model. Figure 8 shows the comparisons of the prediction using viscous potential flow theory with the experimental data of water. The modified model based on viscous potential flow is greatly improved at elevated pressures at which the viscosities of two fluids become comparable [9-13].

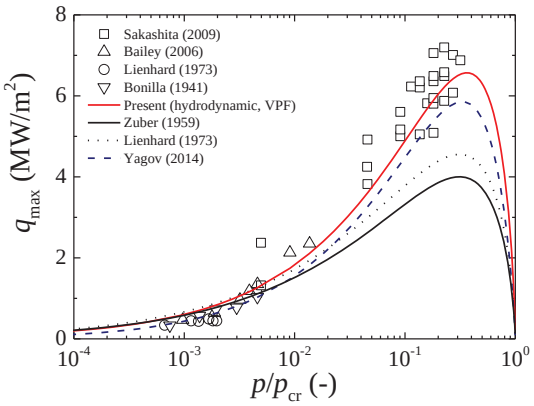


**Figure 8. Comparison of the modified models with experimental data for water**

## 6. DROPLET TWO-GROUP INTERFACIAL AREA TRANSPORT MODEL

In modeling the droplet field, an interfacial area concentration of the droplet is one of crucial parameters to estimate the interfacial momentum and heat transfer between the droplet and vapor phases. Especially, the droplet breakup at spacer grid increases the interfacial area of the droplet and can affect the quenching behavior and the PCT (Peak Cladding Temperature) during a reflood phase. Conventional approach has calculated the interfacial area concentration of the droplet from a droplet size model. This model was based on a non-dimensional Weber number including the effect of the surface tension, which can be available in a sufficiently fully-developed flow condition. However, it is not appropriate to consider the dynamic behavior of the interfacial area of the droplet such as the breakup by the spacer grid.

The SPACE code adopted an IAT (Interfacial Area Transport) model to enhance the prediction capability for the interfacial area of the droplet field. The IAT model for the droplet field estimates the interfacial area concentration by solving the IAT equation, rather than using a static correlation. When the droplet collides on the spacer grid surface, a small droplet can be generated by the breakup, which increases the interfacial area and the amount of droplet evaporation. In particular, the breakup on the spacer grid surface can produce very small droplets, which needs to be distinguished by large droplets [14]. Considering existence of the large and small droplets, two-group IAT equation model was implemented in the SPACE code.

The IAT equation estimates temporal variation of the interfacial area concentration in a given control volume by considering all source terms affecting the droplet size as shown in Eqs. (7) and (8). Equation (7) estimates the variation of the interfacial area concentration for the large droplet ($A_{i,LD}^{'''}$), where the source term in the right-hand-side includes convection of the interfacial area, entrainment/de-entrainment, phase change, and the breakup by the spacer grid. Transport of the interfacial area concentration for the small droplet ($A_{i,SD}^{'''}$) is calculated by Eq. (8). Similar to the large droplet field, the source term for a transport equation of the small droplet is composed of the convection, phase change, and breakup. After calculating the two transport equations, the total interfacial area concentration is estimated as a summation of $A_{i,LD}^{'''}$ and $A_{i,SD}^{'''}$.

$$\frac{\partial A_{i,LD}^{'''}}{\partial t} = -\nabla \cdot \left( A_{i,LD}^{'''} \overline{U}_e \right) + \frac{3S^{'''}}{\rho_l r_s} + S_{\Gamma,LD} + S_{grid} \tag{7}$$

$$\frac{\partial A_{iSD}^{'''}}{\partial t} = -\nabla \cdot \left( A_{iSD}^{'''} \overline{U}_e \right) + S_{\Gamma,SD} + S_{SD1} + S_{SD2} \tag{8}$$

The source term for the droplet breakup in two equations ($S_{grid}$, $S_{SD1}$, $S_{SD2}$) can be modeled taking into account the droplet breakup mechanism as shown in Fig. 9. When a large droplet flow collides with the spacer grid surface, the breakup flow is divided into the source term for the large droplet field and the small droplet field depending on diameter and mass flux of the droplet field. Collision of the small droplet flow with the spacer grid can contribute to the source term of the small droplet field, only if the Weber number of the small droplet field is larger than 30.9. [14]

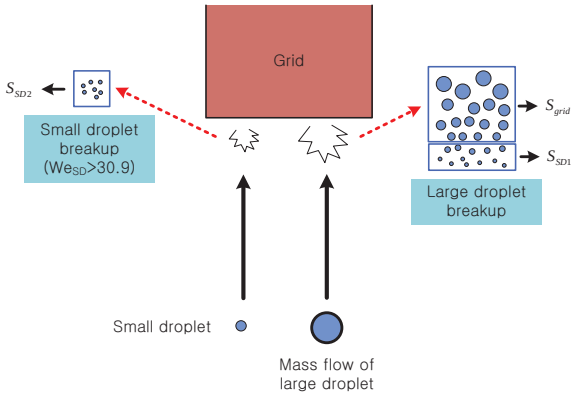


**Figure 9. Breakup mechanism of the droplet field**

## 7. UNCERTAINTY QUANTIFICATION BASED ON DATA ASSIMILATION TECHNIQUE

This section presents data assimilation capabilities for both linear and nonlinear systems to statistically determine the biases and uncertainties of physical models, and subsequently uncertainties on responses. Data assimilation procedure provides the means for integrating a "new" observed data to improve the model's prediction accuracy. It introduces a statistical approach for data adjustment indicating how prior knowledge can be updated by additional experimental data. During the data assimilation procedure, given measurements of the observables and the initial distributions of the model parameters, one calibrates the model based upon Bayes' theorem to achieve better agreement between the measured and predicted values. The calibrated parameter distribution is called the *a posteriori* distribution of the parameters.

Deterministic approach of data assimilation is based upon the distributions of the parameters being Gaussian and the system being linear with respect to the parameters. The solution for the deterministic method is accomplished by differentiating the *a posteriori* distribution of the parameters with respect to the parameter vector and solving it for the calibrated parameter values. To address the nonlinear responses in data assimilation, a sampling approach was employed by propagating the parameter uncertainties through the simulation model to predict the *a posteriori* distributions of the parameters. This is conducted using the Markov Chain Monte Carlo (MCMC) method [15] which seeks to determine the steady-state Markov distribution by generating Markov chains that coincide with the target distribution, i.e., the *a posteriori* distribution of the parameters in our case. MCMC simulation searches the original target distribution by generating sequences of random samples from the target distribution, and subsequently visualizes the distribution utilizing all accepted chains obtained during the simulation.

To estimate uncertainties on the physical models, Bennett's Heated Tube Experiment [16] and Becker's Post Dryout Heat Transfer Experiment [17] were used for the SPACE. Employing the post-CHF experimental data, including measurement errors for each experiment, the *a posteriori* distributions for both parameters and responses were obtained using deterministic and probabilistic methods. Tables 3 and 4 present the physical models and boundary conditions, respectively, that were selected to have their values adjusted through data assimilation.

**Table 3. Physical Models selected for Data Assimilation**

| Index | Physical Models |
|---|---|
| 1 | Interfacial Friction Coefficients between Vapor-Droplet |
| 2 | Interfacial Friction Coefficients for Bubbly Flow |
| 3 | Interfacial Friction Coefficients for Annular Flow |

| | |
|---|---|
| 4 | Heat Transfer Coefficients for Single Phase Liquid |
| 5 | Heat Transfer Coefficients for Single Phase Vapor |
| 6 | Chen Heat Transfer Coefficient - macro |
| 7 | Chen Heat Transfer Coefficient - micro |
| 8 | Critical Heat Flux Model |
| 9 | Minimum Film Boiling Temperature |
| 10 | Interfacial Heat Transfer Coefficient in Annular Regime |
| 11 | Interfacial Heat Transfer Coefficient in Inverted Slug Flow |

**Table I. Boundary Conditions selected for Data Assimilation**

| Boundary Condition Index | Boundary Condition |
|---|---|
| 1 | Mass Flow Rate |
| 2 | Pressure |
| 3 | Temperature |
| 4 | Power |

For the deterministic approach, the inverse problem using regularization and the iteration method to address mild nonlinearity was solved and *a posteriori* values were obtained. For the sampling approach, the MCMC simulation was completed for the wall temperature simulation utilizing Bennett and Becker post-CHF experimental data to compute the *a posteriori* distributions for all parameters and boundary condition values. Uncertainties were observed to be reduced, but non-Gaussian distributions occurred due to the nonlinearity of the system. Parameters influencing the responses most strongly undergo the largest calibration. The results indicate that the optimum models that maximize the uncertainty reduction on the responses are heat transfer coefficients for single phase vapor and critical heat flux model. Figures 10 and 11 show the experimental data together with the *a posteriori* distribution for the wall temperatures obtained using the best estimated physical models/boundary conditions for the sampling method. It is shown that the calibrated response distributions effectively cover the experimental data. The solution for the sampling method was better than that obtained using deterministic approach since the sampling approach does not approximate the responses during the model calibration.

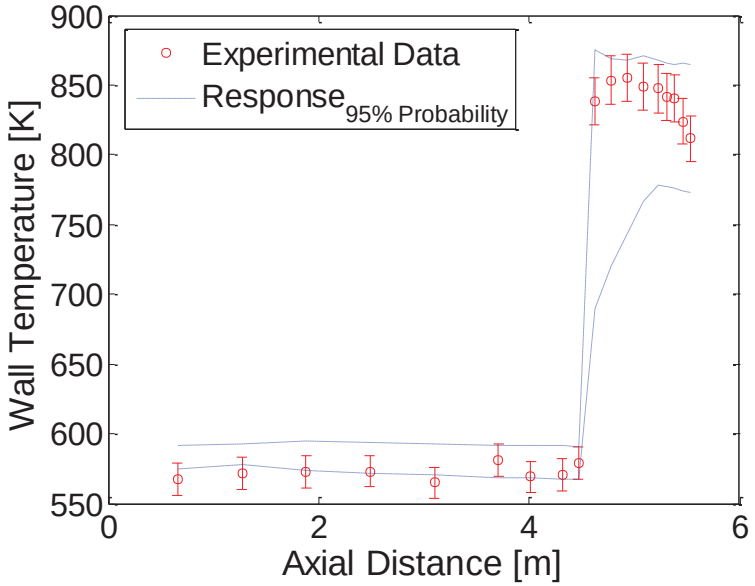


Figure 10. Uncertainty Band of the Experimental Data and Responses for the Bennett Run no. 5312

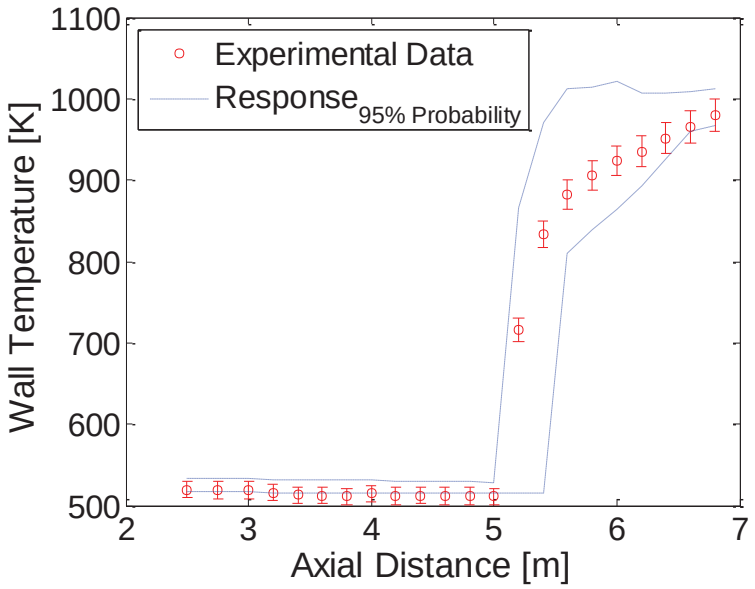


Figure 11. Uncertainty Band of the Experimental Data and Responses for the Becker Run no. 334

In addition to the Bennett and Becker post dryout test, several experimental data were utilized for the uncertainty estimation of the physical models. For example, to enhance predictions of the reflooding phenomena by calibrating models in the simulation code, Flooding Experiments with Blocked Arrays (FEBA) [18] were utilized for data assimilation. For this analysis one determined uncertainty bands of the parameters using FEBA experimental data, and performed blind test for 2D PERICLES [19] test using the *a posteriori* uncertainty information of the parameters. It turned out that not all PERICLES data were within the calibrated temperature distributions due to the scaling up effects. Thus for future work, data assimilation can be expanded to include the scaling issues.

## 8. SUMMARY

SPACE code has been developed to be used for a safety analysis of PWR design. To extend application areas and enhance the calculation accuracy, new features have been implemented which includes multi-dimensional model development and V&V, optional two-phase two-fluid model for fast execution, improved wall drag and from loss treatments to correct nonphysical phasic velocities for a dispersed fields, an improved CHF model for pool boiling condition based on instability theory, a two group interfacial area transport model for droplet, and uncertainty quantification based on data assimilation technique.

## ACKNOWLEDGMENTS

This work was supported by the Nuclear Power Technology Development Program in the form a Korea Institute of Energy Technology Evaluation and Planning (KETEP) grant funded by the Korean Ministry of Knowledge Economy (MKE).

## REFERENCES

1. S. J. Ha, C. E. Park, K. D. Kim, C. H. Ban, "Development of the SPACE Code for Nuclear Power Plant," *Nuclear Engineering and Technology*, **43 (1)**, pp. 45-62 (2011).
2. K.M. Bukhar and R.T. Lahey Jr., "An experimental study of 2-D phase separation phenomena," *Int. J. Multiphase Flow*, **13**(3), pp. 387-402 (1987).
3. B.J. Kim, J.W. Kim, and K.D. Kim, "On the wall drag term in the averaged momentum equation for dispersed flow," Nuclear Science and Engineering **178**, pp. 225-239 (2014).
4. B.J. Kim, S.W. Lee, and K.D. Kim, "New wall drag and form loss models for one-dimensional dispersed two-phase flow," Nuclear Science and Technology, accepted for publication (2015).
5. B.J. Kim, J.H. Kim, and K.D. Kim, "Rayleigh-Taylor instability for thin viscous gas films: Application to critical heat flux and minimum film boiling," International Journal of Heat and Mass Transfer **80**, 150-158 (2015).
6. N. Zuber, *Hydrodynamic aspects of boiling heat transfer (thesis)*, California. Univ., Los Angeles; and Ramo-Wooldridge Corp., Los Angeles, (1959).
7. T. Funada, D.D. Joseph and S. Yamashita, "Stability of a liquid jet into incompressible gases and liquids," *International journal of multiphase flow*, **30**(11), 1279-1310 (2004).
8. C.-K. Guan, J.F. Klausner, R. Mei, "A new mechanistic model for pool boiling CHF on horizontal surfaces," *Int. J. Heat Mass Transfer*, **54,** 3960-3969 (2011).
9. V.V. Yagov, "Is a crisis in pool boiling actually a hydrodynamic phenomenon?," *International Journal of Heat and Mass Transfer*, **73**, 265-273 (2014).
10. J.H. Linehard and V.K. Dhir, *Extended hydrodynamic theory of the peak and minimum pool boiling heat fluxes*, NASA CR-2270, NASA, USA, (1973).
11. W. Bailey, E. Young, C. Beduz and Y. Yang, "Pool boiling study on candidature of pentane, methanol and water for near room temperature cooling," *IEEE*, pp. 599-603 (2006)
12. H. Sakashita and A. Ono, "Boiling behaviors and critical heat flux on a horizontal plate in saturated pool boiling of water at high pressures," *International Journal of Heat and Mass Transfer*,52(3), 744-750 (2009).
13. C.F. Bonilla and C.W. Perry, "Heat transmission to boiling binary liquid mixtures," *Chemical Engineering Progresses Symposium Series*, pp. 685-705 (1941).
14. EPRI, *Analysis of FLECHT-SEASET 163-Rod Blocked Bundle Data Using COBRA-TF*, NUREG/CR-4166 (1985)
15. Nicholas Metropolis, Arianna W. Rosenbluth, Marshall N. Rosenbluth, Augusta H. Teller and Edward Teller, "Equation of State Calculation by Fast Computing Machines," *Journal of Chemical Physics*, **21**(2), pp. 1087-1092, (1953).

16. A. W. Bennett, G. F. Hewitt, H. A. Kearsey and R. K. F. Keeys, *Heat Transfer to Steam –Water Mixtures Flowing in Uniformly Heated Tubes in which the Critical Heat Flux has been Exceeded*, AERE-R5373, (1976).
17. K. M. Becker, C. H. Ling, S. Hedberg and G. Strand, *An Experimental Investigation of Post Dryout Heat Transfer*, Department of Nuclear Reactor Engineering, Royal Institute of Technology, KTH-NEL-33, (1983).
18. P. Ihle and K. Rust, *FEBA – Flooding Experiments with Blocked Arrays Evaluation Report*, Kfk Karlsruhe, Rep. KfK 3657, March (1984).
19. R. Deruaz, P. Clement, and J. M. Veteau, *Study of Two-Dimensional Effects in the Core of a Light Water Reactor During the Reflooding Phase of a LOCA*, Contract no. 002 SRF, (1985).